

Reexamination of wavelength scaling of harmonic yield in intense midinfrared fields

Yunhui Wang,¹ Chao Yu,¹ Qi Shi,¹ Yadong Zhang,¹ Xu Cao,¹ Shicheng Jiang,¹ and Ruifeng Lu^{1,2,*}

¹*Department of Applied Physics, Nanjing University of Science and Technology, Nanjing 210094, People's Republic of China*

²*State Key Laboratory of Molecular Reaction Dynamics, Dalian Institute of Chemical Physics, Chinese Academy of Sciences, Dalian 116023, People's Republic of China*

(Received 12 September 2013; published 18 February 2014)

We theoretically investigate harmonic generation driven by intense midinfrared lasers. A valleylike structure is observed at very low-order harmonics because of a low-energy photoelectron suppression effect. Further, at the beginning of a broad supercontinuum, a convex structure appears that is distributed from the tail in a very narrow energy band in time-frequency maps. Surprisingly, our quantum dynamics calculations demonstrate the beneficial wavelength scaling of the harmonic yield to be $\lambda^{4.6}$ for He and $\lambda^{5.1}$ for Ne over selected energy windows. The bandwidth of the harmonic plateau with only a single quantum trajectory contribution can be further extended by adding a controlling laser field, and the harmonic efficiency is found to be significantly enhanced after macroscopic propagation. In addition, ultrashort isolated attosecond pulses can be obtained by properly superposing the harmonics in the plateaus of both the He and Ne systems.

DOI: [10.1103/PhysRevA.89.023825](https://doi.org/10.1103/PhysRevA.89.023825)

PACS number(s): 42.65.Ky, 33.20.Xx, 34.50.Gb

I. INTRODUCTION

Matter exposed to intense lasers produces a variety of nonlinear phenomena. Among typical phenomena observed in the past two decades, high-order harmonic generation (HHG) is attracting much attention because of its important application to generation of an isolated attosecond pulse (IAP) or a tunable extreme ultraviolet (XUV) femtosecond pulse. The IAP is a powerful tool for probing and manipulating ultrafast electron dynamics in atoms and molecules with unprecedented resolution [1–4]. The harmonic spectrum has unique features: The intensities of several orders are initially very high, and then the harmonic intensity drops sharply and presents a supercontinuum plateau with a sharp cutoff at the end. To broaden the harmonic supercontinuum and to acquire ultrashort attosecond pulses, two-color [5–8] and multicolor laser fields are suggested as useful schemes [9,10]. In fact, the maximal harmonic photon energy is given by the well-known cutoff law $E_{\text{cutoff}} = I_p + 3.17U_p$ [11], and the maximum electric energy is $10U_p$, where I_p denotes the ionization potential of the gas atom or molecule, and U_p is the ponderomotive energy, which is related to the electric field strength E and the fundamental laser frequency ω as $U_p = E^2/4\omega^2$. Furthermore, we can obtain $U_p = E^2\lambda^2/16\pi^2c^2$, in which c is the speed of light, and λ is the laser wavelength. In this expression, a longer fundamental wavelength is beneficial for increasing the ponderomotive potential and harmonic cutoff. The tunneling ionization and multiphoton ionization processes are distinguished by the Keldysh parameter as $\gamma = \sqrt{I_p/2U_p}$. For $\gamma \ll 1$, the tunneling ionization process is a more adequate description than the multiphoton ionization process, whereas for $\gamma \gg 1$, the converse applies. That U_p scales as λ^2 implies that a longer fundamental wavelength for a given laser intensity would drive the laser-matter interaction into the tunneling region.

Most experimental and theoretical research has studied HHG and IAPs by using intense laser pulses from a Ti:sapphire

laser system operating at $\lambda \approx 800$ nm. The recent development of optical parametric amplification (OPA) techniques makes it possible to produce intense, few-cycle laser pulses with midinfrared (MIR) wavelengths between 1500 and 4000 nm [12–16], and higher-energy electrons and harmonics can be generated by MIR lasers. The key issue is the harmonic yield from the long-wavelength MIR laser field produced by OPA techniques compared to the yield from the commonly used 800-nm laser field. Hence, much more attention has been given to the dependence of the HHG yield on λ . It is known that, according to the semiclassical strong-field approximation (SFA), the spreading of the returning wave packet produces a λ^{-3} dependence of the HHG efficiency [17], and experiments have provided partial support for this theoretical result [18]. However, the harmonic efficiency ($\lambda^{-6.3 \pm 1.1}$ in Xe and $\lambda^{-6.5 \pm 1.1}$ in Kr for wavelengths of 800–1850 nm) decreases more rapidly in experimental measurements than in numerical predictions [19]. Additional outstanding work has been done in experiment [20–23] and in theory [24–32] to reveal the harmonic yield dependence on λ . Investigations of the photon yield based on the single-atom response and SFA show that the yield in He beyond the 1-keV energy range can be increased by some orders of magnitude using long-wavelength driving sources in the range of 1.5 to 3 μm [24]. Wavelength scaling of the HHG from a near-visible 800-nm to an MIR 2000-nm fundamental pulse in an intense electromagnetic field has been reported by solving the quantum mechanical (QM) time-dependent Schrödinger equation (TDSE) for argon and by using the SFA for helium. These methods indicate that the harmonic yield follows a $\lambda^{-(5-6)}$ scaling at constant intensities [25]. The much faster decrease in the harmonic yield has encouraged researchers to explore further details of the λ dependence for higher-order returning quantum trajectory interference [26–29]. The $\lambda^{-(5-6)}$ scale of the harmonic yield has been reproduced [30,31], and the oscillations on that scale are thought to be of quantum origin involving threshold phenomena, which are sensitive to the bound-state wave function's symmetry [30]. By combining an 800-nm assistant field with an infrared fundamental field, the yield scaling can be slowed from $\lambda^{-(5-6)}$ to $\lambda^{-(3-4)}$ [31]. A study of XUV-assisted HHG [32] shows that the harmonic

*rflu@njust.edu.cn

yield is almost independent of the wavelength of the driving laser. That study claims that the wavelength scaling of the harmonic yield is not simply governed by the wave-packet spreading ($\propto \lambda^{-3}$) [17] and the apparent energy distribution effect ($\propto \lambda^{-2}$) [26,27] but exhibits richer and more complex behaviors.

Motivated by the different wavelength dependence behaviors, this paper presents a theoretical investigation that reexamines the fundamental wavelength scaling of the harmonic yield for He and Ne atoms interacting with intense MIR lasers. Numerical analyses are conducted in both single-color and two-color fields. We also carefully consider the macroscopic propagation effects and compare the QM and SFA results to elucidate the underlying mechanism.

II. THEORETICAL METHOD

In our quantum wave-packet calculations, numerically solving the three-dimensional (3D) TDSE is performed by the parallel computer code LZH-DICP [33]. Atomic units and linearly polarized laser fields along the z axis are used throughout the paper. In the single-active-electron and dipole approximations, the 3D TDSE is

$$i \frac{\partial}{\partial t} \psi(\mathbf{r}, t) = \left[-\frac{1}{2} \nabla^2 + V(\mathbf{r}) + H_{\text{int}}(\mathbf{r}, t) \right] \psi(\mathbf{r}, t), \quad (1)$$

where $V(r) = -1/\sqrt{\alpha + r^2}$ is the soft Coulomb potential with parameters $\alpha = 0.484$ and 0.667 corresponding to the exact ionization energy $I_p = 24.6$ eV and 21.56 eV for He and Ne atoms, respectively. H_{int} accounts for the laser-atom interaction $H_{\text{int}}(\mathbf{r}, t) = \mathbf{r} \cdot \mathbf{E}(t) \cos \omega t$, with laser frequency of ω and the laser field of $E(t)$. The 3D TDSE can be solved in spherical coordinates, which leads to a set of coupled partial differential equations, and the evolution of the electronic wave function is advanced using a second-order split-operator approach. After determining the time-dependent wave function, the time-dependent induced dipole acceleration can be obtained by $d_A(t) = \langle \psi(r, t) | -\frac{\partial V(r)}{\partial r} + E(t) | \psi(r, t) \rangle$. The HHG spectra can be calculated by a Fourier transformation of the time-dependent induced dipole acceleration $P_A(t) = |\frac{1}{\sqrt{2\pi}} \int_0^t d_A e^{-i\omega t} dt|^2$, and then the IAPs are obtained by superposing several harmonics $I(t) = |\sum_q (\int_0^t d_A e^{-i\omega t} dt) e^{-iq\omega t}|^2$, where q is the harmonic order.

The harmonic spectrum can also be given by the Lewenstein model [18], which is based on the SFA, and the instantaneous dipole moment of an atom is described as

$$\begin{aligned} d_{nl} = & i \int_{-\infty}^t dt' \left[\frac{\pi}{\varepsilon + i(t-t')/2} \right]^{3/2} \mathbf{d}^*[\mathbf{p}_{st}(t', t) - \mathbf{A}(t)] \\ & \times \mathbf{d}[\mathbf{p}_{st}(t', t) - \mathbf{A}(t')] \exp[iS_{st}(t', t)] \\ & \times \mathbf{E}(t' - t) g^*(t') g(t' - t) + \text{c.c.} \end{aligned} \quad (2)$$

In this equation, $\mathbf{A}(t)$ is the vector potential, ε is a positive regularization constant, and $g(t) = \exp[-\int_{-\infty}^t W(t'') dt'']$ —which is introduced to account for depletion of the ground state—represents the ground-state amplitude, where $W(t'')$ is the ionization rate obtained by the Ammosov-Delone-Krainov

theory [34]. $\mathbf{p}_{st}(t', t) = \frac{1}{t-t'} \int_{t'}^t \mathbf{A}(t'') dt''$ is the canonical momentum at the stationary points, and $S_{st}(t', t) = (t-t')I_p - \mathbf{p}_{st}^2(t', t)(t-t')/2 + \int_{t'}^t \mathbf{A}^2(t'') dt''/2$ is the quasiclassical action at the stationary points.

Macroscopic propagation effects are considered through a self-consistent solution to the TDSE and Maxwell wave equation (MWE). To investigate the copropagation of the laser and harmonics beams, we take the single-atom response computed from 3D TDSE as the source term for the 3D MWE. The propagation of the fundamental laser and of harmonics beams in the ionizing gas is governed by the two equations

$$\nabla^2 E_l(\rho', z', t) - \frac{1}{c^2} \frac{\partial^2 E_l(\rho', z', t)}{\partial t^2} = \frac{\omega_p^2(\rho', z', t)}{c^2} E_l(\rho', z', t), \quad (3)$$

$$\begin{aligned} \nabla^2 E_h(\rho', z', t) - \frac{1}{c^2} \frac{\partial^2 E_h(\rho', z', t)}{\partial t^2} \\ = \frac{\omega_p^2(\rho', z', t)}{c^2} E_h(\rho', z', t) + \mu_0 \frac{\partial^2 P(\rho', z', t)}{\partial t^2}, \end{aligned} \quad (4)$$

where ρ' and z' are, respectively, the longitudinal and transverse coordinates of an atom in the interaction gas medium, and E_l and E_h are, respectively, the laser and harmonic fields. ω_p is the plasma frequency given by $\omega_p(\rho', z', t) = [\frac{e^2 n_e(\rho', z', t)}{\varepsilon_0 m_e}]^{1/2}$, and $P(\rho', z', t) = [n_0 - n_e(\rho', z', t)] d_n(\rho', z', t)$ is the nonlinear polarization generated by the gas medium. $n_e = n_0 W_{\text{ion}}$ is the free-electron density in the gas, and n_0 is the gas density. Dipole moment d_n and ionization probability W_{ion} can be obtained from the prior plane via 3D TDSE. This model accounts for both temporal plasma-induced phase modulation and spatial plasma lensing effects on the laser pulse. By moving the coordinate frame and using the paraxial approximation, these equations can be solved using the finite-difference method after a Fourier transform in the frequency domain. The numerical procedures have been clearly described in the literature [35–40]. Our test calculations for a Ne atom reproduced simulated and experimental results [35] very well.

III. RESULTS AND DISCUSSION

The use of an MIR laser for high-efficiency HHG seems to be disappointing; however, the low-energy photoelectron suppression effect [41] has been observed in photoelectron spectroscopy, which demonstrates low electron ionization in the low-frequency region. Low-order harmonics are almost always generated from low-energy electrons. Consequently, when the yield of near-zero-momentum electrons in the strong-field tunneling ionization regime is significantly suppressed, a very small harmonic yield appears in the elliptical area in Fig. 1. To confirm this result, we calculated the HHG of He in MIR laser fields from 0.95 to $2.55 \mu\text{m}$ at a constant driving laser intensity of $5.7 \times 10^{14} \text{ W/cm}^2$; we present the results at example wavelengths of 1.4 , 1.6 , and $1.8 \mu\text{m}$ in Fig. 1. From this figure, we can see that the harmonic yield in the low-frequency region was remarkably reduced and formed a deep valley, and the neighboring high-frequency region is clearly divided into two parts: a convex part with higher intensities

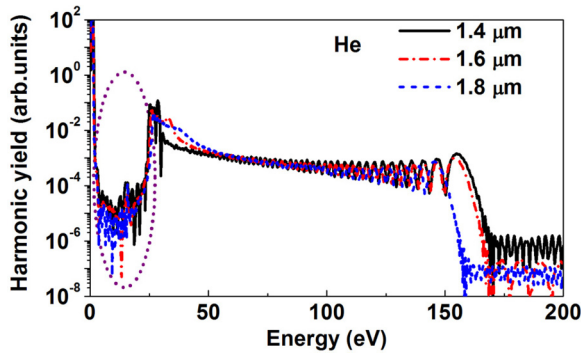


FIG. 1. (Color online) HHG spectra of He atom in single 6-fs laser field with peak intensity of 5.7×10^{14} W/cm² and wavelengths of 1.4, 1.6, and 1.8 μ m.

in the relatively low-photon-energy region and an ultrabroad regular plateau in the high-energy region. Furthermore, we note that the right edge of the convex portion is extended, and the efficiency around this edge increases roughly with increasing wavelength.

To better understand the physics behind the special valley-like structure in the harmonic spectra's low-frequency region, a wavelet time-frequency analysis was performed, as shown in Fig. 2. There is almost no photon energy distribution below 25 eV, which directly generates the valleylike structure. It is well known that a trajectory with an earlier ionization time and a later recombination time is called a long path, and a trajectory with a later ionization time and an earlier recombination time is called a short path. The two branches of the peak correspond to the so-called long and short paths. Figure 2 illustrates clearly that the long quantum path is selected and the short path is strongly suppressed, which prevents destructive interference. Only the long quantum path contributes to the spectra above 25 eV, which results in a plateau with a bandwidth of 130 eV. A comparison with Fig. 1 reveals that the tail from one optical cycle (T_0) to $1.5T_0$ is responsible for the high-intensity convex region next to the valley. This means that the slow electrons having nearly the same energy recombine with the parent ion

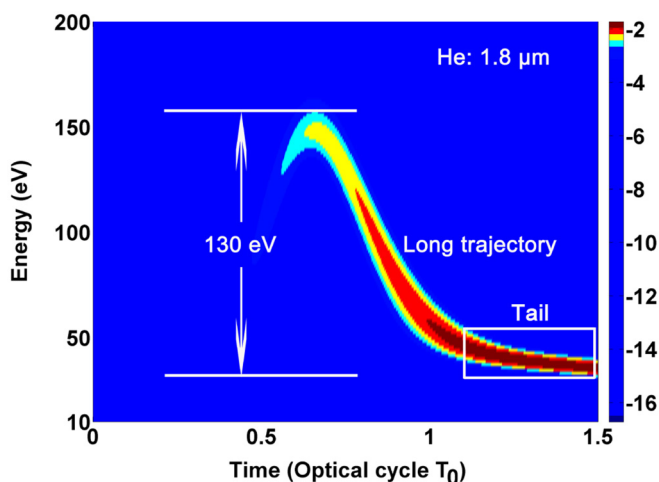


FIG. 2. (Color online) Wavelet time-frequency profile corresponding to wavelength of 1.8 μ m in Fig. 1.

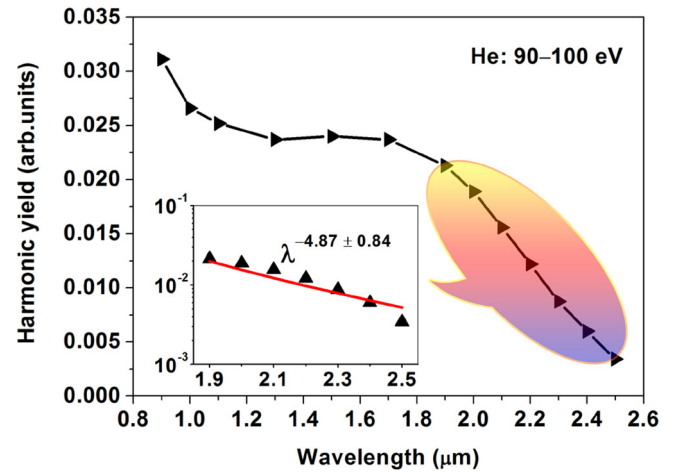


FIG. 3. (Color online) Wavelength dependence of integrated harmonic yield from 90 to 100 eV at wavelengths of 0.95–2.55 μ m for a He system.

in half of an optical cycle, producing a relatively low-energy convex structure from 25 to about 50 eV.

The above valuable findings motivated us to further explore the wavelength dependence of HHG from near-visible (0.95 μ m) to MIR (2.55 μ m) wavelengths using a single He or Ne atom exposed to an intense laser field with a laser intensity of 5.7×10^{14} W/cm². We first examined the wavelength scaling of the harmonics generated by the interaction of He gas with a single intense laser. Figure 3 depicts the integrated harmonic yield from 90 to 100 eV. The harmonic yield has a monotonic decreasing trend following the increase in the driving laser's wavelength. More specifically, the harmonic yield initially declines rapidly; then an area of smooth change appears, with a dramatic decrease again after 1.7 μ m. The inset in Fig. 3 indicates that the HHG yield scales as $\lambda^{-4.87}$, which is consistent with previous investigations [25,26,28,31].

The wavelength scaling law is evaluated in more detail by integrating the harmonic yield from 25 to 35 eV. As shown in Fig. 4(a), the harmonic yield curve can be divided into three sections. The first decreasing range (from 0.95 to 1.05 μ m), the increasing range (from 1.05 to 1.55 μ m), and the more rapidly decreasing range (from 1.05 to 2.55 μ m) are marked as regions I, II, and III, respectively. In Figs. 4(b) and 4(c), the wavelength scaling is fitted to be $\lambda^{3.92}$ and $\lambda^{-2.97}$ for regions II and III, respectively. The wavelength dependence in region III is consistent with the theoretically predicted dependence of the HHG efficiency according to the semiclassical SFA [17]. The result that particularly drew our notice occurs in region II, which contradicts both experimental observation and a previous theoretical prediction. This region suggests a promising possibility for enhancing the harmonic yield using only a single intense MIR laser. Furthermore, the wavelength scaling dependences at higher photon energies of 35–45 eV and 60–70 eV were also evaluated and are displayed in Figs. 5 and 6, respectively.

The trend observed in Fig. 4(a) can be found in Figs. 5(a) and 6(a). Compared with Fig. 4(b), a marked enhancement in region II is realized at a wider wavelength range. A wavelength scaling increase to $\lambda^{4.59}$ (1.1 μ m to 1.85 μ m)

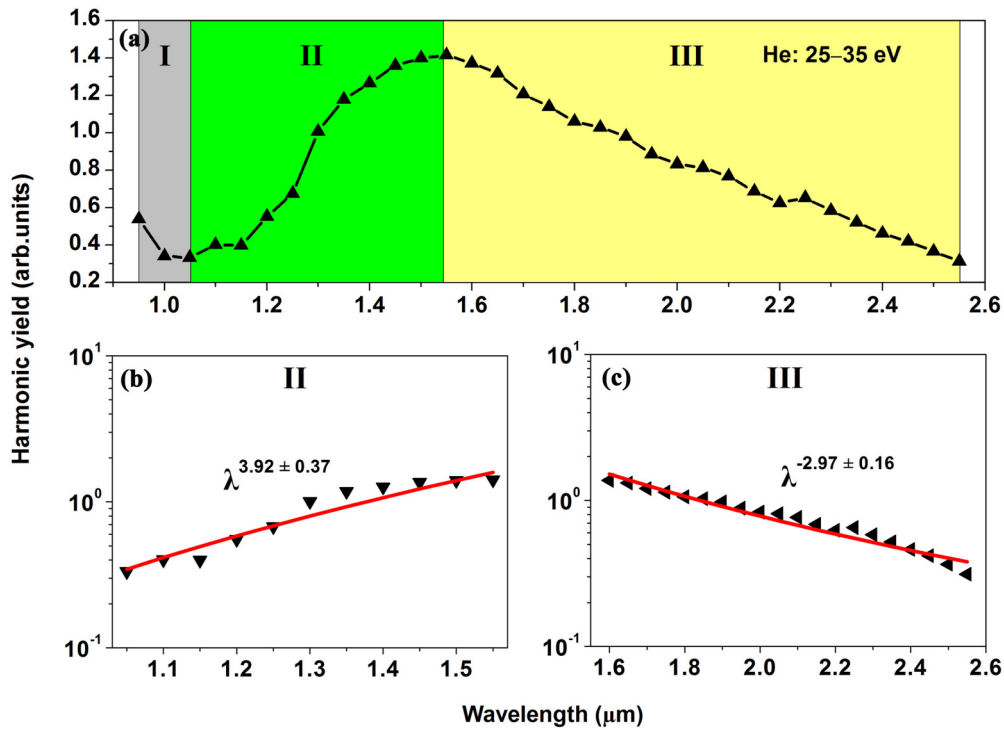


FIG. 4. (Color online) (a) Wavelength dependence of integrated harmonic yield from 25–35 eV at wavelengths of 0.95–2.55 μm for a He system, and wavelength scaling in (b) region II and (c) region III.

for 35–45 eV is shown in Fig. 5(b). In Fig. 6(b), the rate of increase is slower, and the wavelength scaling is $\lambda^{1.01}$ for 60–70 eV, whereas region II (1.1–1.95 μm) is larger than region II in Fig. 5(a). In Figs. 5(c) and 6(c), the

wavelength scaling in region III decreases to $\lambda^{-4.62}$ and $\lambda^{-5.90}$, respectively; this finding shows that, with increasing wavelength, the harmonic yields decline more quickly than in Fig. 4(d). The very unfavorable values of $\lambda^{-4.62}$ and $\lambda^{-5.90}$

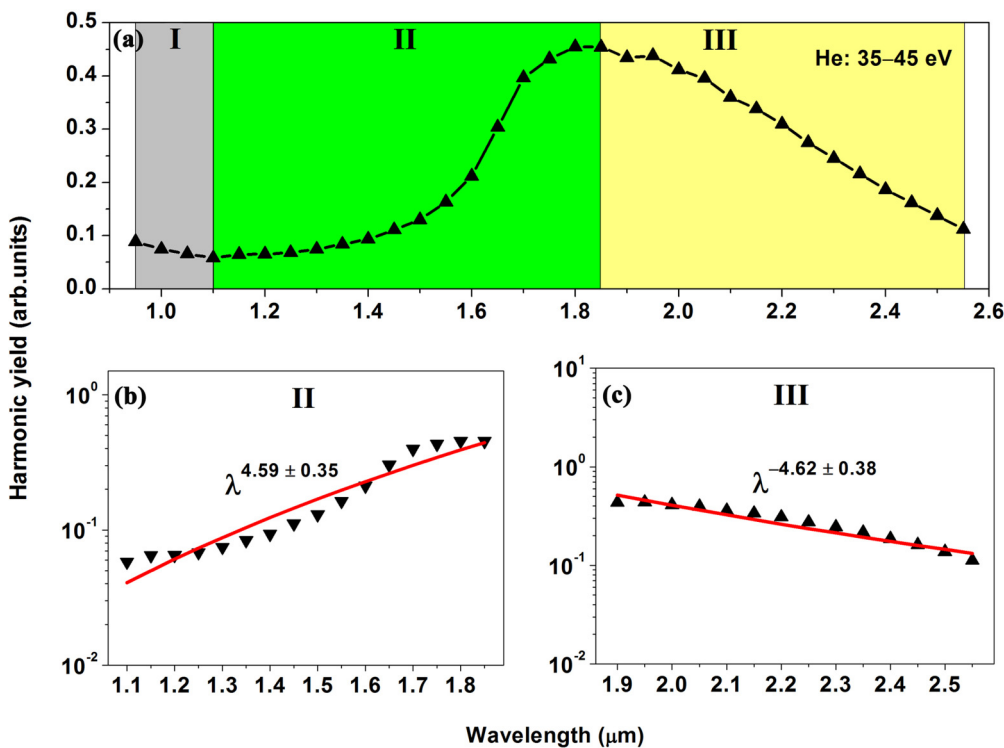


FIG. 5. (Color online) (a) Wavelength dependence of integrated harmonic yield from 35 to 45 eV at wavelengths of 0.95 μm to 2.55 μm for a He system, and wavelength scaling in (b) region II and (c) region III.

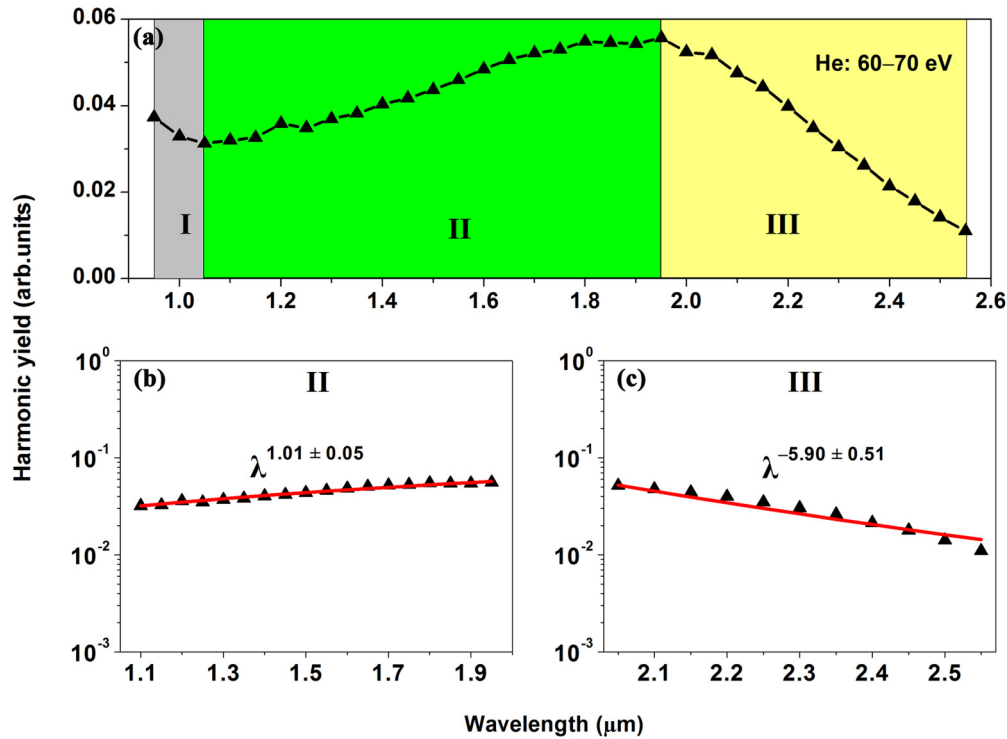


FIG. 6. (Color online) (a) Wavelength dependence of integrated harmonic yield from 60 to 70 eV at wavelengths of 0.95–2.55 μm for a He system, and wavelength scaling in (b) region II and (c) region III.

are consistent with recent numerical studies predicting $\lambda^{-(5-6)}$ [25,31].

Although we do not provide data for all energy ranges, a qualitative trend appears: With increasing harmonic energy, region II broadens below 80 eV and then shrinks at larger energies (no such “region II” exists for energies greater than 100 eV), whereas region III shrinks monotonically, and the harmonic yields in region III decrease much more rapidly, approaching the wavelength scaling in experiments. From Figs. 1 and 2, we confirm that the unexpected region II originates straightforwardly from the above-mentioned low-energy photoelectron suppression effect accompanying the formation of a high-intensity convex region in the harmonic plateau. The explanation of the shrinkage (and eventually disappearance) of region II at large harmonic energies is quite understandable in that the high-energy harmonics beyond the convex area are affected little by the low-energy photoelectron suppression effect. Therefore, the beginning of the plateau deserves more attention, and the better wavelength scalings of $\lambda^{3.92}$, $\lambda^{4.59}$, and $\lambda^{1.01}$ provide an opportunity to increase the HHG efficiency by applying intense MIR lasers in future experiments.

Additionally, the two-color field scheme was also considered in this study, with a peak laser intensity of $5.7 \times 10^{14} \text{ W/cm}^2$ for the synthesized two-color pulse. More specifically, a peak intensity of $3.4 \times 10^{14} \text{ W/cm}^2$ was used for the 6-fs driving pulse with a wavelength varying from 0.95 to 2.55 μm , and a peak intensity of $3.0 \times 10^{13} \text{ W/cm}^2$ was used for the 9-fs controlling pulse with a wavelength of 1.6 μm (this is denoted briefly as the 6+9 scheme). For comparison, we take the results of a 1.8- μm driving laser as an example; as shown in Fig. 7(a), the valleylike structure

in the very-low-frequency region and the convex structure at the beginning of the plateau can still be observed in the harmonic spectrum. In addition, we note that there is an obvious peak at 15.83 eV in this valley. To our knowledge, a similar peak appears in the harmonic spectra for molecular LiH^{3+} and is attributed to virtual states [42]. To address the underlying mechanism generating the sharp peak in the valley, supplementary HHG from the SFA [17] (using the same laser parameters as in the QM calculations) is added in Fig. 7(a). We see that the peak in the valleylike structure disappears when the SFA method is applied. Because the contributions from all bound states—except for the ground state for HHG—are neglected in the SFA approach [17], we can infer that this peak may originate from other bound states. Furthermore, we notice that the transition energy from the He atom’s ground state to its first excited state is 15.88 eV, which matches this peak’s position very well. The time-dependent probabilities for the ground state and first excited state in Fig. 8 show that the electronic state population prefers the ground state and first excited state over other highly bound states with very small values (not shown here). The coupling between the ground state and first excited state results in low-frequency photons and valleylike structures. Thus, we believe that the first excited state contributes to the peak generation in the valley.

Comparing the result from a single laser field in Fig. 1 at 1.8 μm to that from the two-color laser field scheme in Fig. 7(a), we find that the harmonic plateau is broadened by about 30 eV and the long quantum path can still be selected, as shown in Fig. 7(b). Because the ionized gas medium will cause a distortion and phase shift in the laser pulse after propagation [43], and because macroscopic effects may significantly change the single-atom results [36], we

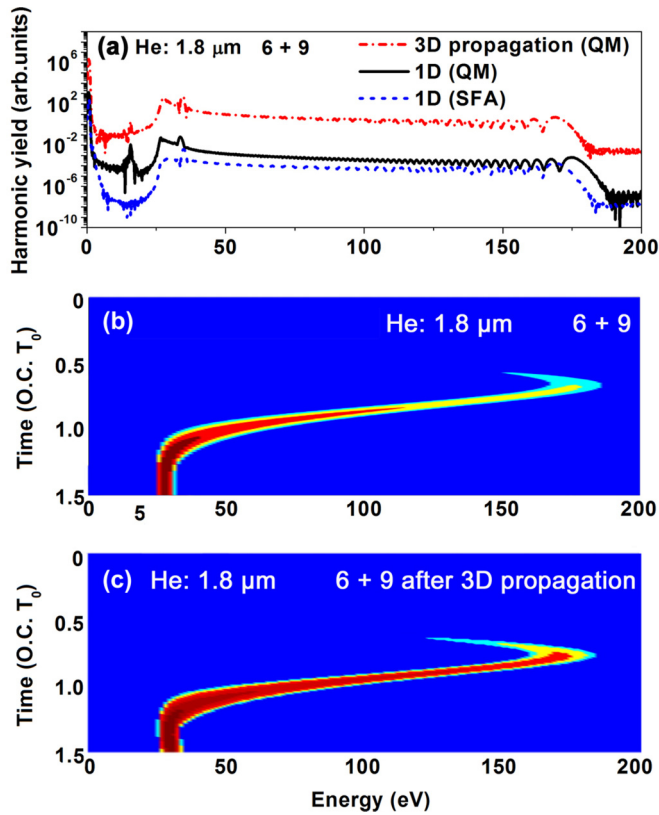


FIG. 7. (Color online) (a) Harmonic spectra from solution to TDSE based on single-atom response (black solid line) and after 3D propagation (red dash-dot line) by QM method, and harmonic spectra from SFA method (blue dashed line) in 6 + 9 two-color scheme for He system. Corresponding time-frequency analyses for (b) single-atom response and (c) macroscopic propagation. Wavelength of driving laser is 1.8 μm .

investigated the influence of the 3D propagation effect on the harmonic field in the gas target. The results indicate that the HHG yield over the entire spectral range is enhanced by four orders of magnitude after macroscopic propagation, whereas the overall profile (including the valleylike and convex structures) almost reproduces the profile for the single-atom response. The harmonic field is the coherent sum of the radiation from all the molecules in the gas and is a result of constructive interference, mostly in the forward direction; thus, the increasing HHG yield is due mainly to phase matching during propagation [36]. After propagation in the medium, the single quantum path can also be chosen, as illustrated in the time-frequency analysis map in Fig. 7(c).

To confirm this beneficial wavelength scaling in another gas, we calculated the HHG for a Ne atom, using the same parameters (a single strong laser) as for the He system. The harmonic spectrum and corresponding time-frequency analysis in Fig. 9 present similar valleylike and convex structures, an ultrabroad plateau, and a selected single long quantum path, as in the He system in the MIR laser field. This similarity encouraged us to continue exploring the wavelength scale of the Ne system. The harmonic yield's wavelength scaling integrated from 32 to 42 eV is displayed in Fig. 10. The overall trend of the high-order harmonic yield for wavelengths

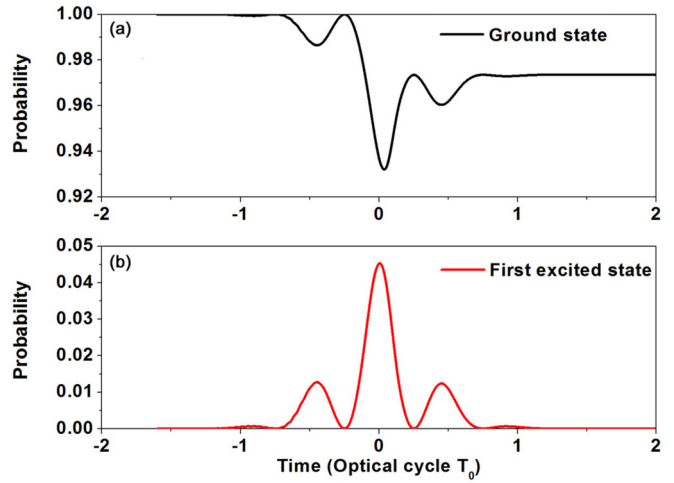


FIG. 8. (Color online) Time-dependent populations for (a) ground state and (b) first excited state of 6 + 9 scheme. Laser parameters are identical to those in Fig. 7.

from 950 nm to 2.55 μm in Fig. 10(a) can also be divided into the initial declining section (I), the second enhancement section (II), and the third declining section (III). In Fig. 10(b), the wavelength scaling is $\lambda^{5.12}$ in region II, and $\lambda^{-3.74}$ is obtained for region III. Although the medium is different, there still exists a wavelength window for faster harmonic yield enhancement; thus, the universal wavelength scaling for both the He and Ne systems requires careful reexamination and can be used to obtain high-intensity HHG with MIR laser techniques.

By superposing the harmonics from the 38th to the 254th order in Fig. 7(a) for the 6 + 9 two-color scheme, an isolated 25.5-as pulse can be obtained, as shown in Fig. 11. Moreover, isolated 31.7-as and 32.2-as pulses can be derived from a single 1.8- μm driving laser by superposing the harmonics from the 38th to the 212th order for He and from the 34th to the 206th order for Ne, respectively. From the results for

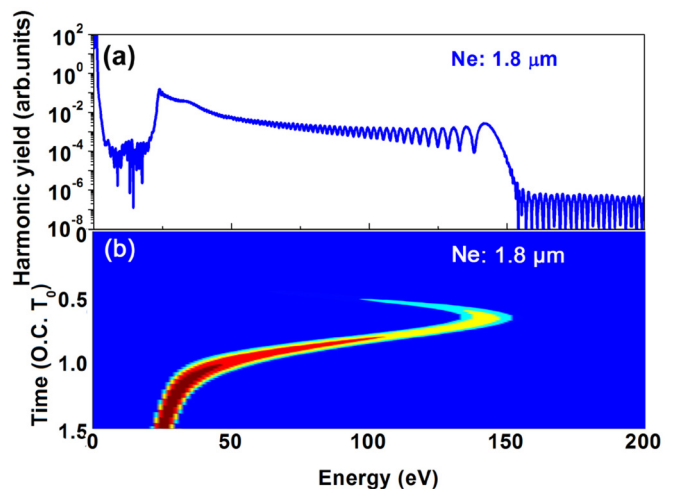


FIG. 9. (Color online) (a) Harmonic spectra at wavelength of 1.8 μm for Ne system, and (b) corresponding time-frequency analysis. Laser wavelength is 1.8 μm , and other parameters are identical to those in Fig. 1.

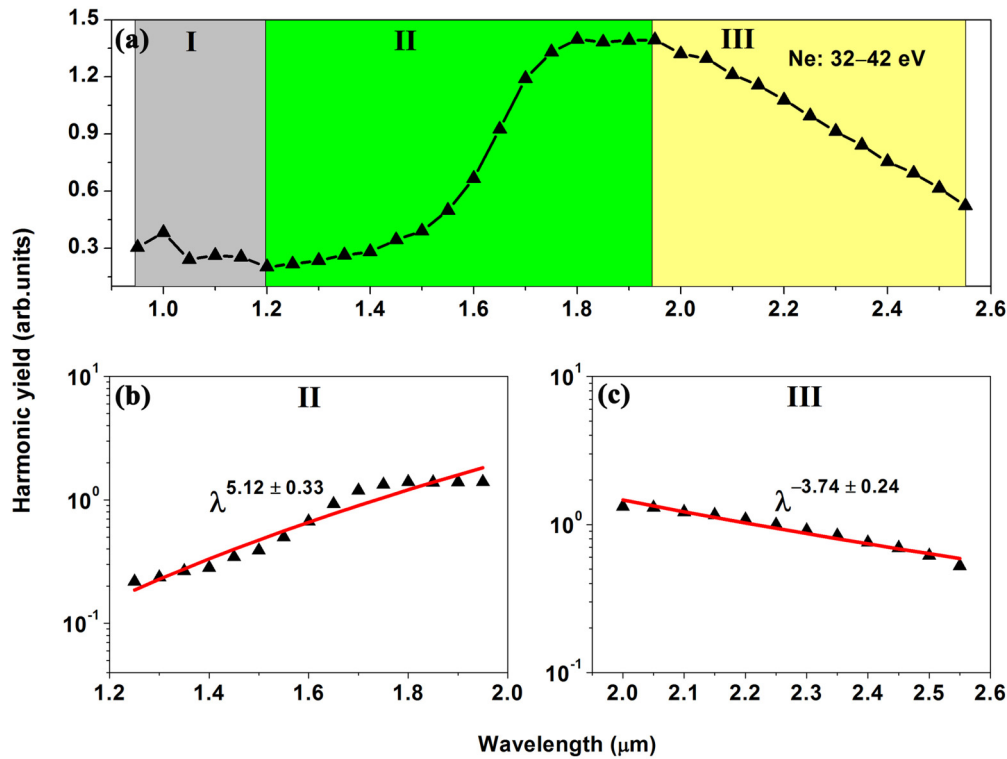


FIG. 10. (Color online) (a) Wavelength dependence of integrated harmonic yield from 32 to 42 eV at wavelengths of 0.95–2.55 μm for a Ne system, and wavelength scaling in (b) region II and (c) region III.

the He system, the two-color scheme both produces a shorter IAP and also improves the intensity of the IAP under the same peak intensity as the single laser. We emphasize that the temporal profiles of the attosecond pulses are calculated without any phase compensation. The pulse duration of the IAP from the 6 + 9 scheme approaches the atomic unit of time (24 as). Such an ultrashort pulse offers a new window for observing ultrafast electronic dynamics with unprecedented time resolution. Although laser parameters, including the carrier-envelope phase, frequency, and intensity of both the driving and controlling pulses, affect HHG (and these factors have been investigated in detail in our previous work [44]

and elsewhere in the literature [38,45,46]), this work's main finding—that the harmonic yield's wavelength scaling should be reexamined—remains unchanged.

IV. CONCLUSIONS

In conclusion, we investigated HHG by He and Ne atoms exposed to intense MIR laser fields with both the QM and SFA methods. The observed valleylike structure has been reported in the low-frequency region of harmonic spectra owing to low-energy photoelectron suppression, and the mechanism generating the sharp peak in the valley is studied in detail. Moreover, the convex structure appearing at the beginning of the broad atomic plateau is ascribed to photon emission in a narrow low-energy range after one optical cycle of the interacting laser. More importantly, we carefully explored the harmonic yield's wavelength dependence in MIR driving laser fields, and our results demonstrate a marked enhancement in a relatively wide wavelength window. The harmonic yield's positive wavelength scaling paves the way to the production of high-intensity HHG using MIR lasers. We further considered the two-color scheme and macroscopic propagation; the high-intensity ultrashort IAP obtained in this work shows promise for furthering attosecond science.

ACKNOWLEDGMENTS

This work was supported by NSF of China Grants No. 11004107 and No. 21373113, and the Scientific Research Innovation Projects of Jiangsu Province for University Graduate Students with Grant No. CXZZ13_0201.

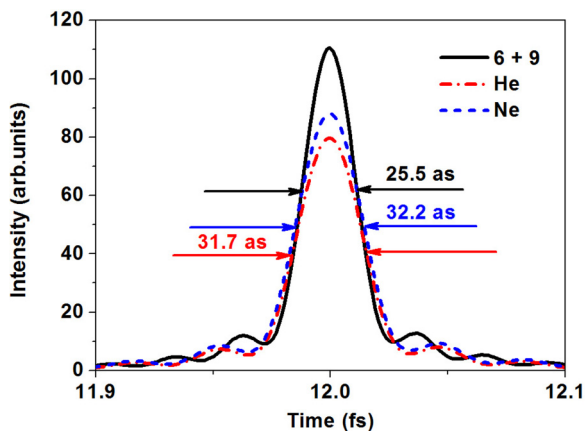


FIG. 11. (Color online) IAPs generated using 6 + 9 scheme (black solid line) for He and a single 6-fs laser field for He (blue dashed line) and Ne (red dash-dot line). Wavelength of driving laser is 1.8 μm .

- [1] G. Mourou and T. Tajima, *Science* **331**, 41 (2011).
- [2] M. Uiberacker, Th. Uphues, M. Schultze, A. J. Verhoef, V. Yakovlev, M. F. Kling, J. Rauschenberger, N. M. Kabachnik, H. Schröder, M. Lezius, K. L. Kompa, H.-G. Muller, M. J. J. Vrakking, S. Hendel, U. Kleineberg, U. Heinzmann, M. Drescher, and F. Krausz, *Nature* **446**, 627 (2007).
- [3] P. B. Corkum and F. Krausz, *Nat. Phys.* **3**, 381 (2007).
- [4] R. Kienberger, E. Goulielmakis, M. Uiberacker, A. Baltuška, V. Yakovlev, F. Bammer, A. Scrinzi, Th. Westerwalbesloh, U. Kleineberg, U. Heinzmann, M. Drescher, and F. Krausz, *Nature* **427**, 817 (2004).
- [5] A. D. Bandrauk, S. Chelkowski, H. Yu, and E. Constant, *Phys. Rev. A* **56**, R2537 (1997).
- [6] Y. Oishi, M. Kaku, A. Suda, F. Kannari, and K. Midorikawa, *Opt. Express* **14**, 7230 (2006).
- [7] T. Pfeifer, L. Gallmann, M. J. Abel, D. M. Neumark, and S. R. Leone, *Opt. Lett.* **31**, 975 (2006).
- [8] W. F. Yang, X. H. Song, S. Q. Gong, Y. Cheng, and Z. Z. Xu, *Phys. Rev. Lett.* **99**, 133602 (2007).
- [9] R. F. Lu, H. X. He, Y. H. Guo, and K. L. Han, *J. Phys. B: At. Mol. Opt. Phys.* **42**, 225601 (2009).
- [10] G. Orlando, P. P. Corso, E. Fiordilino, and F. Persico, *J. Phys. B: At. Mol. Opt. Phys.* **43**, 025602 (2010).
- [11] J. L. Krause, K. J. Schafer, and K. C. Kulander, *Phys. Rev. Lett.* **68**, 3535 (1992).
- [12] B. Sheehy, J. D. D. Martin, L. F. DiMauro, P. Agostini, K. J. Schafer, M. B. Gaarde, and K. C. Kulander, *Phys. Rev. Lett.* **83**, 5270 (1999).
- [13] T. Fuji, N. Ishii, C. Y. Teisset, X. Gu, Th. Metzger, A. Baltuška, N. Forget, D. Kaplan, A. Galvanauskas, and F. Krausz, *Opt. Lett.* **31**, 1103 (2006).
- [14] C. Vozzi, G. Cirmi, C. Manzoni, E. Benedetti, F. Calegari, G. Sansone, S. Stagira, O. Svelto, S. De Silvestri, M. Nisoli, and G. Cerullo, *Opt. Express* **14**, 10109 (2006).
- [15] C. P. Hauri, R. B. Lopez-Martens, C. I. Blaga, K. D. Schultz, J. Cryan, R. Chirila, P. Colosimo, G. Doumy, A. M. March, C. Roedig, E. Sistrunk, J. Tate, J. Wheeler, L. F. DiMauro, and E. P. Power, *Opt. Lett.* **32**, 868 (2007).
- [16] C. Vozzi, F. Calegari, E. Benedetti, S. Gasilov, G. Sansone, G. Cerullo, M. Nisoli, S. De Silvestri, and S. Stagira, *Opt. Lett.* **32**, 2957 (2007).
- [17] M. Lewenstein, Ph. Balcou, M. Yu. Ivanov, A. L'Huillier, and P. B. Corkum, *Phys. Rev. A* **49**, 2117 (1994).
- [18] B. Shan and Z. Chang, *Phys. Rev. A* **65**, 011804(R) (2001).
- [19] A. D. Shiner, C. Trallero-Herrero, N. Kajumba, H. C. Bandulet, D. Comtois, F. Légaré, M. Giguère, J. C. Kieffer, P. B. Corkum, and D. M. Villeneuve, *Phys. Rev. Lett.* **103**, 073902 (2009).
- [20] B. Mahieu, S. Coraggia, C. Callegari, M. Coreno, G. De Ninno, M. Devetta, F. Frassetto, D. Garzella, M. Negro, C. Spezzani, C. Vozzi, S. Stagira, L. Poletto, *Appl. Phys. B* **108**, 43 (2012).
- [21] P. Colosimo, G. Doumy, C. I. Blaga, J. Wheeler, C. Hauri, F. Catoire, J. Tate, R. Chirila, A. M. March, G. G. Paulus, H. G. Muller, P. Agostini, and L. F. DiMauro, *Nat. Phys.* **4**, 386 (2008).
- [22] E. J. Takahashi, T. Kanai, Y. Nabekawa, and K. Midorikawa, *Appl. Phys. Lett.* **93**, 041111 (2008).
- [23] E. L. Falcão-Filho, C.-J. Lai, K.-H. Hong, V.-M. Gkortsas, S.-W. Huang, L.-J. Chen, and F. X. Kärtner, *Appl. Phys. Lett.* **97**, 061107 (2010).
- [24] A. Gordon and F. X. Kärtner, *Opt. Express* **13**, 2941 (2005).
- [25] J. Tate, T. Augustine, H. G. Muller, P. Salières, P. Agostini, and L. F. DiMauro, *Phys. Rev. Lett.* **98**, 013901 (2007).
- [26] K. Schiessl, K. L. Ishikawa, E. Persson, and J. Burgdörfer, *Phys. Rev. Lett.* **99**, 253903 (2007).
- [27] K. Schiessl, K. L. Ishikawa, E. Persson, and J. Burgdörfer, *J. Mod. Opt.* **55**, 2617 (2008).
- [28] K. L. Ishikawa, K. Schiessl, E. Persson, and J. Burgdörfer, *Phys. Rev. A* **79**, 033411 (2009).
- [29] T. Augustine, F. Catoire, P. Agostini, L. F. DiMauro, C. C. Chirila, V. S. Yakovlev, and P. Salières, *New J. Phys.* **14**, 103014 (2012).
- [30] M. V. Frolov, N. L. Manakov, and A. F. Starace, *Phys. Rev. Lett.* **100**, 173001 (2008).
- [31] P. F. Lan, E. J. Takahashi, and K. Midorikawa, *Phys. Rev. A* **81**, 061802(R) (2010).
- [32] K. L. Ishikawa, E. J. Takahashi, and K. Midorikawa, *Phys. Rev. A* **80**, 011807(R) (2009).
- [33] R. F. Lu, P. Y. Zhang, and K. L. Han, *Phys. Rev. E* **77**, 066701 (2008).
- [34] M. V. Ammosov, N. B. Delone, and V. P. Krainov, *Zh. Eksp. Teor. Fiz.* **91**, 2008 (1986).
- [35] E. Priori, G. Cerullo, M. Nisoli, S. Stagira, S. De Silvestri, P. Villoresi, L. Poletto, P. Ceccherini, C. Altucci, R. Bruzese, and C. de Lisio, *Phys. Rev. A* **61**, 063801 (2000).
- [36] M. B. Gaarde, J. L. Tate, and K. J. Schafer, *J. Phys. B: At. Mol. Opt. Phys.* **41**, 132001 (2008).
- [37] C. Altucci, V. Tosa, and R. Velotta, *Phys. Rev. A* **75**, 061401(R) (2007).
- [38] C. Altucci, J. W. G. Tisch, and R. Velotta, *J. Mod. Opt.* **58**, 1585 (2011).
- [39] H. C. Du and B. T. Hu, *Phys. Rev. A* **84**, 023817 (2011).
- [40] H. C. Du, Y. Z. Wen, X. S. Wang, and B. T. Hu, *Opt. Express* **21**, 21337 (2013).
- [41] H. Liu, Y. Q. Liu, L. B. Fu, G. G. Xin, D. F. Ye, J. Liu, X. T. He, Y. D. Yang, X. R. Liu, Y. K. Deng, C. Y. Wu, and Q. H. Gong, *Phys. Rev. Lett.* **109**, 093001 (2012).
- [42] L. Q. Feng and T. S. Chu, *Commun. Comput. Chem.* **1**, 52 (2013).
- [43] M. Geissler, G. Tempea, A. Scrinzi, M. Schnürer, F. Krausz, and T. Brabec, *Phys. Rev. Lett.* **83**, 2930 (1999).
- [44] Y. H. Wang, H. P. Wu, Y. Qian, Q. Shi, C. Yu, Y. Chen, K. M. Deng, and R. F. Lu, *J. Mod. Opt.* **59**, 1640 (2012).
- [45] G. J. Zhao, X. L. Guo, T. J. Shao, and K. Xue, *New J. Phys.* **13**, 093035 (2011).
- [46] V. Tosa, C. Altucci, K. Kovács, M. Negro, S. Stagira, C. Vozzi, and R. Velotta, *IEEE J. Sel. Top. Quantum Electron.* **18**, 239 (2012).